

# **Characterizing Tissue Graft Angiogenesis via Multimodal Optical Imaging**

by

**Adam L Mendez**

*A thesis submitted to Johns Hopkins University in conformity with the  
requirements for the degree of Masters of Science in Engineering in  
Chemical and Biomolecular Engineering*

Baltimore, Maryland

May, 2018

## ABSTRACT

Tissue engineered scaffolds are a powerful means of healing craniofacial bone defects arising from trauma or disease. Murine models of critical-sized bone defects are especially useful in understanding the role of microenvironmental factors such as vascularization on bone regeneration. In this thesis, we review the previously employed bone graft methods used to treat orthopedic tissue defects, the transition of therapeutic approaches to tissue engineering based regimes, and the various imaging modalities which may be used to characterize osteogenesis and angiogenesis within defect sites. Additionally, we demonstrate the capability of a novel multimodality imaging platform capable of acquiring *in vivo* images of microvascular architecture, microvascular blood flow and tracer/cell tracking via intrinsic optical signaling (IOS), laser speckle contrast (LSC) and fluorescence (FL) imaging, respectively in a critical-sized calvarial defect model. Defects that were 4 mm in diameter were made in the calvarial regions of mice followed by the implantation of osteoconductive scaffolds loaded with human adipose-derived stem cells (ASCs) embedded in fibrin gel. Using IOS imaging, we were able to visualize microvascular angiogenesis at the graft site and extracted morphological information such as vessel radius, length, and tortuosity two weeks after scaffold implantation. FL imaging allowed us to assess functional characteristics of the angiogenic vessel bed such as time-to-peak of a fluorescent tracer, and also allowed us to track the distribution of fluorescently tagged human umbilical vein endothelial cells (HUVECs). Finally, we employed LSC to characterize the *in vivo* hemodynamic response and maturity of the remodeled microvessels in the scaffold microenvironment. In this thesis, we provide a methodical framework for imaging tissue engineered scaffolds, processing the images in order to extract key microenvironmental parameters, and visualizing this data in a manner that enables the characterization of the vascular phenotype and its effect on bone regeneration. Such multimodality imaging platforms can inform optimization and design of tissue engineered scaffolds and elucidate the factors that promote enhanced vascularization and bone formation.

### **Primary advisor and reader**

Dr. Arvind Pathak  
Russell H. Morgan Department of Radiology and  
Radiological Science  
Johns Hopkins University School of Medicine

### **Secondary advisor and reader**

Dr. Warren Grayson  
Department of Biomedical Engineering  
Johns Hopkins University

## ACKNOWLEDGEMENTS

First and foremost, I'd like to thank Dr. Arvind Pathak and Dr. Warren Grayson who gave me the knowledge and education in a field I was previously unfamiliar with as well as the skills and work ethic that I will use going forward. I'd also like to thank Dr. Janaka Senarathna and Dr. Akanksha Bhargava for everything they taught me throughout this past year and all of their help on this project. I'd like to thank Lexi Rindone for her help on this project and the writing that pushed this work to publication, as well as Pegah Abbasnia who I unfortunately never got to work with, but contributed to the early design of this project. I'd like to thank our retired lab manager Stacy Gil for showing me the ropes when I first joined the lab and Namrata Batra who's work kickstarted this project. And finally I'd like to thank all the other members of the Pathak lab which include Elysia Gao, Gayatri Susarla, Dr. Qihong Wang, George Anderson, Callie Deng, and Darian Hadjiabadi for their friendship and support throughout the course of the project.

## LIST OF ABBREVIATIONS

<b>Abbreviation</b>	<b>Explanation</b>
<i>ASC</i>	Adipose Derived Stem Cell
<i>BMP</i>	Bone Morphogenetic Protein
<i>DMEM</i>	Dulbecco's Modified Eagle's Medium
<i>DCE-MRI</i>	Dynamic Contrast Enhanced – Magnetic Resonance Imaging
<i>DSC-MRI</i>	Dynamic Susceptibility Contrast - Magnetic Resonance Imaging
<i>ESC</i>	Embryonic Stem Cell
<i>EDM</i>	Euclidean Distance Map
<i>FITC</i>	Fluorescein Isothiocyanate
<i>FL</i>	Fluorescence Imaging
<i>FoV</i>	Field of View
<i>HUVEC</i>	Human Umbilical Vein Endothelial Cell
<i>I</i>	Mean pixel intensity
<i>IOS</i>	Intrinsic Optical Signal
$I_o$	Incident Light
$I_a$	Reflected Light
<i>iPSC</i>	Induced Pluripotent Stem Cell
<i>K</i>	Speckle contrast
<i>L</i>	Path Length of Light Traveled
<i>LSC</i>	Laser Speckle Contrast
<i>MIP</i>	Maximum Intensity Projection
<i>MSC</i>	Mesenchymal Stem Cell
<i>OCT</i>	Optical Coherence Tomography
<i>PCL</i>	Polycaprolactone
<i>PET</i>	Positron Emission Tomography
<i>RFP</i>	Red Fluorescence Protein
<i>SNR</i>	Signal to Noise Ratio
<i>T</i>	Exposure Time
<i>V</i>	Velocity
<i>VEGF</i>	Vascular Endothelial Growth Factor
<i>[X]</i>	Concentration of Species X
$C\tau$	Temporal Average of Intensity Autocorrection Function
$\tau$	Decorrelation Time
$\mu$	Absorption Coefficient
$\mu CT$	Micro Computed Tomography
$\sigma$	Standard Deviation
$\gamma$	Wavelength of Light

## LIST OF FIGURES

<b>Item</b>	<b>Caption</b>	<b>Page</b>
<i>Fig. 1</i>	<p>In vivo imaging of the calvarial defect model. (a) Benchtop multi-contrast optical imaging system used to acquire in vivo images of the microenvironment of engineered scaffolds implanted in a calvarial defect model. (b). Diagram of the calvarial defect area location on a mouse skull. (c) Superior view of a 3D-printed polycaprolactone scaffold implanted in the calvarial defect. (d) Magnified view of 4 mm 3D printed scaffold seeded with ASCs suspended in a fibrin gel. (Calvarial Diagram adapted from: Zhang W, Zhu C, Ye D, Xu L, Zhang X, Wu Q, et al. Porous Silk Scaffolds for Delivery of Growth Factors and Stem Cells to Enhance Bone Regeneration. PLoS ONE. 2014;9(7):1.)</p>	5
<i>Fig. 2</i>	<p>Fig. 2: Multi-contrast in vivo imaging of the graft microenvironment. Flow chart illustrating key microenvironmental factors that are interrogated in vivo (green) within the calvarial defect site; the in vivo optical contrast mechanism employed (red) to assay these factors; the imaging method employed (blue), and the metrics computed for characterizing the in vivo graft microenvironment. * Can also be used to track fluorescently labeled stem cell survival and location.</p>	16
<i>Fig. 3</i>	<p>Fig. 3: Analysis of vascular morphology in the in vivo graft microenvironment. (a) IOS image of the calvarial defect site two weeks after implantation wherein the vasculature is dark due to green light absorption. PCL scaffold is outlined by the gray circle. (b) LSC image of the same FoV wherein perfused blood vessels appear bright due to red laser light being scattered by moving erythrocytes. PCL scaffold is again outlined by a gray circle. (c, d) Images in (a, b) overlaid with their respective binary vessel masks. (e) Combination of the vessel masks in (c, d) to provide a holistic mask of all the vessels that are visible using either imaging method. (f) Map of the average vessel radius</p>	22

corresponding to the vessel segments identified in (e). (g, h, i) Distribution of vessel characteristics for the sample shown in (e).

*Fig. 4* Fig. 4: Analysis of tracer kinetics and cell distribution in the in vivo graft 24  
microenvironment. (a) Representative time series of fluorescent images  
acquired after injection of the fluorescent intravascular tracer FITC-dextran.  
PCL scaffold is outlined by the large gray dashed circles.(b) Plot of the  
fluorescence intensity from the ROI (red circle) in (a) illustrating the transit of  
the intravascular tracer through the vasculature within the graft. Red points  
correspond to the time points for which snapshots are shown in (a). (c) Time-to-  
peak (TTP) map computed from the tracer data for each vessel segment within  
the FoV. (d) Fluorescent image of a scaffold seeded with a mixture of ASCs  
and red fluorescent protein (RFP) labeled HUVECs (red channel) illustrating  
the utility of the fluorescent channel for cell tracking.

*Fig. 5* Figure 5: Analysis of perfusion and vessel maturity in the in vivo graft 25  
microenvironment. (a) Baseline blood flow map (normalized to the maximum  
flow across all samples). (b) Normalized blood flow map generated by  
computing the average blood flow during the carbogen inhalation periods. (c)  
Map of the percent change in blood flow induced by carbogen inhalation. More  
mature blood vessels exhibit larger changes in blood flow. Note only positive  
changes are displayed. (d) LSC image indicating ROI (red circle) corresponding  
to the blood flow time course in (e). PCL scaffold is outlined by gray circle.  
Time series were baseline corrected and only positive perfusion changes were  
plotted. The robust response to carbogen inhalation in (e) during the 240-300 s  
(blue bar) and 540-600 s (blue bar) intervals indicate the degree of maturity of  
the blood vessels within the red circle in (d). (f) Vessel classification of  
carbogen response in (c) using k means clustering. Vessels appearing as red are  
those that indicated the greatest degree in blood flow change while black  
indicates the lowest change. (g) Probability distribution function of change in  
blood flow in response to carbogen as seen in (f). (h) Probability distribution

function of vessel radii according to the same classifications in (g) and (f). The lack in variability across vessel sizes indicates that radius had no effect on carbogen response. (i) Similar distribution as seen in (h) but with the time to peak of each vessel. Again, the lack in variability indicates a lack of a relationship between carbogen response and time to peak response following injection of the dextran-FITC tracer.

# TABLE OF CONTENTS

Content	Page
<b>LIST OF ABBREVIATIONS</b> .....	iv
<b>LIST OF FIGURES</b> .....	v
<b>CHAPTER 1: FUNDAMENTALS OF ORTHOPEDIC TISSUE ENGINEERING</b> .....	1
1.1 Bone and Muscle Defects and the need for orthopedic tissue engineering.....	1
1.2 Preclinical models for studying bone defects .....	1
1.2.1 <i>Critical Sized Defects</i> .....	2
1.2 The relationship between Angiogenesis and Osteogenesis.....	2
1.3 Tissue Engineering Approaches and Regenerative Medicine.....	3
1.3.1 <i>Stem Cell Overview</i> .....	3
1.3.2 <i>Current Treatment Methods for critical-sized segmental bone defects</i> .....	4
<b>CHAPTER 2: IMAGING TECHNIQUES FOR VISUALIZING VASCULAR AND BONE REMODELING</b> .....	6
2.1 In vivo vs. Ex vivo Imaging .....	6
2.2 Imaging vascular morphology .....	7
2.2.1 <i>Optical sectioning techniques</i> .....	7
2.2.2 <i>Widefield and confocal microscopy</i> .....	7
2.2.3 <i>Intrinsic Optical Signaling, Multiphoton, OCT, and micro-CT</i> .....	8
2.3 Monitoring Hemodynamic Response .....	9
2.3.1 <i>LSC, DCE-MR, and DSC-MR Imaging</i> .....	10
2.3.2 <i>Administration of vasodilators to map vascular maturity and compliance</i> .....	10
2.4 Vascular tracer kinetics and stem cell tracking .....	11
2.4.1 <i>Fluorescence Imaging</i> .....	11
2.4.2 <i>Positron emission tomography</i> .....	11
2.5 Bone Visualization .....	12
2.5.1 <i>X-ray (radiography) and Micro-Computed Tomography</i> .....	12



2.5.2 <i>Ultrasound Imaging</i> .....	12
<b>CHAPTER 3: EXPERIMENTAL PROTOCOL AND IMAGING PROCESSING</b> .....	14
3.1 3D scaffold fabrication .....	14
3.2 Stem cell isolation and calvarial defect preparation.....	14
3.3 Multimodal Imaging Acquisition .....	15
3.3.1 <i>IOS</i> .....	16
3.3.2 <i>FL</i> .....	17
3.3.3 <i>LSC</i> .....	17
3.4 Image Processing Methods.....	18
3.4.1 <i>Resampling Fixed Time Points and Image Registration</i> .....	18
3.4.2 <i>Smoothing, Gaussian, and Low-Pass Filters</i> .....	19
3.4.3 <i>Gaussian and Hessian Filter for distinguishing vessels</i> .....	19
3.4.4 <i>Thresholding and Particle Filtration</i> .....	19
3.4.5 <i>Euclidean Distance Maps and Tagged Skeletons</i> .....	20
<b>CHAPTER 4: ANALYZING VASCULAR REMODELING DATA</b> .....	22
4.1 Results .....	22
4.2 Discussion.....	26
<b>CHAPTER 5: CONCLUSIONS AND FUTURE RESEARCH</b> .....	28
<b>CHAPTER 6: BIBLIOGRAPHY</b> .....	29

# **CHAPTER 1: FUNDAMENTALS OF ORTHOPEDIC TISSUE ENGINEERING**

## **1.1 Bone defects and the need for orthopedic tissue engineering**

Tissue engineering provides a powerful means for repairing defects in bone which result from trauma. Through the introduction osteogenic material, coupled with the appropriate biochemical cues, mechanical stimulation, or growth factors, tissue engineering therapeutics can initiate bone and vascular remodeling, facilitating the healing of bone defect sites (1-3). Such therapeutics have the potential to regenerate tissue in nonunion sites, and critical-sized bone defects, which may enable mobility and functionality in previously unusable injured areas.

## **1.2 Preclinical models for studying bone defects**

Traditional treatments for bone defects arising from trauma include either allogenic or autologous bone grafts. But these treatments do come with inherent advantages and disadvantages. Allogenic bone grafts incorporate the osteoconductive and osteoinductive properties needed to recruit progenitor cells and provide a suitable environment for bone repair through the transplantation of healthy tissue from a donor. However these grafts do not include any osteogenic material, capable of differentiating into new osteoblasts or osteocytes and include a risk of an immune response (4). Because autologous grafts are taken from the host, they prevent the possibility of an immune response, but may result in serious morbidity at the site from which the graft is harvested as well as limitations in tissue available for transplantation (5). Recently, tissue engineering has arisen as a viable alternative to circumvent the issues associated with these traditional bone graft treatments. Tissue engineering involves the design of custom scaffolds, seeded with stem cells, and biochemical factors to provide the needed osteoconductivity, osteogenic material, and osteoinductivity that enables bone regeneration in a safe and cost effective manner (5). To study the regenerative potential of tissue engineered scaffolds in bone defects, preclinical models become necessary. By analyzing the impact of types and concentrations of osteogenic materials in various tissue engineering approaches, the design and safety of materials can be optimized in preclinical models before translating them into

patients. Murine models are well suited for such bone tissue engineering purposes (6, 7) and for imaging stem cell facilitated vascular remodeling *in vivo* (8, 9). Since most tissue engineering studies focus on the use of human stem cells, immunodeficient mice are especially effective models as they do not exhibit graft rejection at the host site (10). To determine the effectiveness of engineering approaches in regenerating orthopedic tissue, an ideal model should focus on a defect that does not demonstrate spontaneous or complete healing without the aid of treatment. These injuries also present the greatest challenge due to a limited number of reconstructive options available (11) and are defined as critical-sized defects (CSD) for bone.

### *1.2.1 Critical Sized Defects*

According to the international standards developed by the ASTM *Standard Guide for Preclinical in vivo Evaluation in Critical Sized Segmental Bone Defects* (F2721-09), a critical-sized bone defect is defined as a defect from which an animal will exhibit “less than ten percent bony healing ten years after the initial injury without any intervention” (12). Characterizations of these defects vary according to animal species, age, anatomical location, and size. However, as an empirical rule, the length of the defect must be at least twice the diameter of the bone (13, 14). Critical-sized defects in murine models have been previously studied in multiple anatomical locations including femoral segmental defects, maxillary defects, and calvarial defects (6, 7, 15). For this thesis, we will focus on calvarial defects. Also known as the “skullcap”, the calvarium is comprised of the neurocranium, which can in turn be divided into the cranial base, chondrocranium, and cranial vault, and the viscerocranium (16). These regions serve to surround and protect the brain as well as form the base structures for the facial skeleton. Due to the anatomical location of this site, typical critical-sized defects used to study tissue engineering-based bone formation include four millimeter (4 mm) circular defects (17, 18).

## **1.3 The relationship between angiogenesis and osteogenesis**

Angiogenesis and osteogenesis are closely coupled processes during tissue regeneration. The co-localization of blood vessels and osteoprogenitor cells allows for the creation of suitable metabolic and biochemical environments that enable enhanced progenitor cell survival, proliferation and differentiation (19). Additionally, blood vessels provide the nutrient and

oxygen deposition needed to foster bone growth (20). In animal models, vascular endothelial growth factor (VEGF), a key signaling protein for guiding the branching and anastomosis of developing vessels, has also been shown to enhance osteogenesis in low doses (19, 21). Recently, the identification of a new blood vessel subtype, Type H, in the metaphysis region of long bones has elucidated some of the previously unknown signaling steps in angiogenesis-osteogenesis cascade. The type H endothelial cells that make up these blood vessels have been found to mediate growth of local vasculature and upregulate important osteogenic factors through the *Notch* signaling pathway (22). For these reasons, tissue engineering approaches should seek to facilitate remodeling of both, the damaged vascular network and bone reformation when treating critical-sized defects.

## **1.4 Tissue engineering approaches and regenerative medicine**

The goal of tissue engineering and regenerative medicine is to stimulate the body's natural regenerative capabilities through the introduction of mechanical or biochemical factors and to provide suitable angiogenic and osteogenic material to reform and replace lost tissue. For this reason, nearly all tissue engineering approaches now incorporate stem cells.

### *1.4.1 Stem Cell Overview*

Stem cells are a powerful means regenerating lost tissue due to their availability and capacity to differentiate into nearly any cell type if provided with the proper environment and growth factors (23). Stem cells can be categorized into three types based on their source: adult stem cells, embryonic stem cells (ESCs), and induced pluripotent stem cells (iPSCs). Types of adult stem cells include hematopoietic, mesenchymal, neural, epithelial, adipose and skin stem cells (24). Embryonic stem cells are derived from the inner cell mass of an embryo 3-5 days after fertilization, and exhibit potential to differentiate into almost any cell type (25). More recently, human umbilical vein endothelial cells (HUVECs) have also been resected from the endothelium of umbilical cord veins after childbirth and used in tissue engineering approaches because of their potential to regulate angiogenesis through interactions with other enzymes and small binding proteins (26). iPSCs are stem cells created in the laboratory setting through the introduction of embryonic genes into a somatic cell, causing them to revert back to a pluripotent

state (27). Their source origin and therefore varying phenotype is commonly identified using the antigen binding of markers to cell surface glycoproteins, classification determinants (CDs). When designing tissue engineering approaches, the type of stem cell must be chosen carefully because different stem cell subtypes will more readily differentiate into subsequent lineages when given stimulatory factors. Many tissue engineering approaches that seek to promote bone reformation use mesenchymal stem cells (MSCs) due to their osteogenic properties and high rate of differentiation in the presence of osteoconductive materials such as bone morphogenetic protein (BMP) (28, 29). More recently, adipose-derived stem cells (ASCs) have also been investigated as a potential source of osteoconductive material due to their osteogenic potential and wider availability compared to MSCs (30).

#### *1.4.2 Current treatment methods for critical-sized segmental bone defects*

Standard treatment procedures for critical-sized, segmental bone defects involve the use of either autografts through vascularized bone transfer or cortical and cancellous bone allografts. However, these approaches are not without serious limitations such as donor site morbidity, a limited supply of graft tissue material, risk of an immune response and variable graft efficacy due to differences in donor bone quality (31). Due to the challenge associated with treating critical-sized defects, and the disadvantages of these traditional methods, limited efficacy has been seen in long term follow up studies of patient trials (32, 33). As such, there is a clear need for tissue engineered therapeutics that circumvent issues associated with conventional grafts and permit the healing of severe orthopedic tissue injuries. In this thesis, we aimed to characterize the vascular remodeling within a critical-sized defect in the calvarial region of mice implanted with a 3D printed polycaprolactone (PCL) scaffold seeded with human ASCs embedded in a fibrin gel medium. To analyze this vascular remodeling, we imaged the defect site two weeks after scaffold implantation using a custom built multimodal imaging system. Our system enabled intrinsic optical signaling (IOS) imaging, fluorescence (FL) imaging, and laser speckle contrast (LSC) imaging during a single experimental session in order to provide information on various aspects of angiogenesis. These imaging methods will be described in detail in Chapter 2. A setup of our imaging system is illustrated in **Fig. 1**.

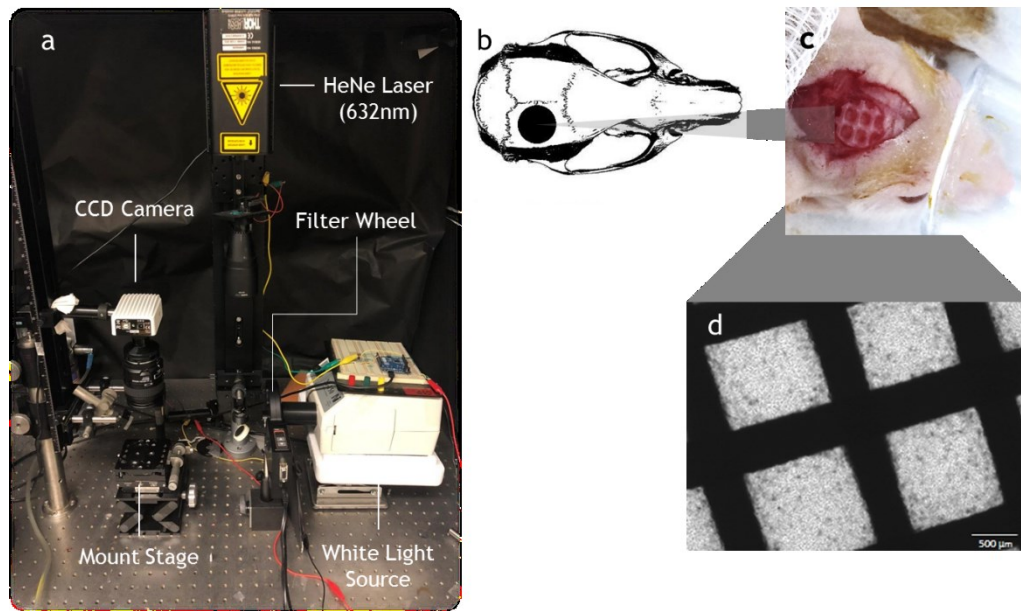


**Fig. 1: In vivo imaging of the calvarial defect model.** (a) Benchtop multi-contrast optical imaging system used to acquire in vivo images of the microenvironment of engineered scaffolds implanted in a calvarial defect model. (b). Diagram of the calvarial defect area location on a mouse skull. (c) Superior view of a 3D-printed polycaprolactone scaffold implanted in the calvarial defect. (d) Magnified view of 4 mm 3D printed scaffold seeded with ASCs suspended in a fibrin gel. (Calvarial Diagram adapted from: Zhang W, Zhu C, Ye D, Xu L, Zhang X, Wu Q, et al. Porous Silk Scaffolds for Delivery of Growth Factors and Stem Cells to Enhance Bone Regeneration. PLoS ONE. 2014;9(7):1.)

## CHAPTER 2: IMAGING TECHNIQUES FOR VISUALIZING VASCULAR AND BONE REMODELING

### 2.1 *In vivo* vs. *Ex vivo* Imaging

Imaging is a powerful tool for characterizing the extent of bone and blood vessel regeneration in clinical and preclinical tissue engineering applications. By visualizing the angiogenic vascular network and bone formation in the defect site, we can quantitatively assess the effect of the stem cell mediated therapy on wound healing at the injury site. This section describes the types of imaging modalities that can be used as well as the quantitative information that can be extracted from each modality. One could employ *in vivo* or *ex vivo* imaging methods to assess angiogenesis and osteogenesis in preclinical bone injury models. *In vivo* imaging is advantageous in such models because it allows for the visualization of the native environment with minimal disturbance to the site. Additionally, *in vivo* imaging techniques provide important information about the dynamic characteristics of blood vessels during the angiogenic process. Since visualization of vessels and bone is often limited by the penetration depth of incident light, maintaining spatial resolution at increased imaging depths becomes challenging (34). *Ex vivo* imaging techniques can be advantageous in studying preclinical models because they often include staining and clearing techniques that improve visualization of the sample and allow for the clear distinguishing of vascular structures, often in 3D (35). Recently, *ex vivo* samples have been used to study retinal angiogenesis in mice (36). The disadvantages of *ex vivo* imaging stem from the fact that they require excision of the imaged samples, which may damage the tissue. Additionally, *ex vivo* imaging cannot be used to study vascular perfusion and the scope of experiments can be limited by the amount of time required to perform the optical clearing and staining of tissue samples. For the purpose of our studies, we chose to utilize *in vivo* imaging techniques to avoid the damage that can occur to tissue samples during excision or tissue clearing procedures, which would result in aberrations throughout imaging (37).

## **2.2 Imaging vascular morphology**

To assess vascular remodeling in bone defect sites, imaging techniques that enable visualization at microvascular spatial resolution (~5-10  $\mu\text{m}$ ) are needed. Such techniques include widefield and confocal microscopy, intrinsic optical signaling, multiphoton microscopy, optical coherence tomography (OCT), and micro-computed tomography (micro-CT). Optical imaging techniques often include optical sectioning to provide depth-resolved 3D images along with the administration of fluorescent dyes to augment visual contrast.

### *2.2.1 Optical sectioning techniques*

Optical sectioning is not its own type of imaging modality, but instead a process by which 3D structures can be visualized without the need for physical sectioning of the tissue being imaged into thin slices. By removing the out-of-focus light within images across multiple focal planes, optical sectioning provides much greater contrast and allows for 3D reconstruction of specimens via the combination of all image planes into a single stack of images (38). This process is implemented in many types of optical imaging such as standard confocal, line scanning, spinning-disk, and multiphoton microscopy in order to increase resolution along the z axis, and is commonly implemented by introducing a pinhole aperture. By placing a pinhole aperture in front of the detector, most of the scattered and out-of-focus light can be eliminated without impeding the light from the desired in-focus plane (38). As such, the pinhole's effectiveness is directly correlated to its size and must be chosen carefully to maintain effectiveness without compromising the difference in brightness between the signal and the background that is needed to distinguish structures. Optical sectioning techniques have recently been utilized to study regeneration in rat femoral defects (39) and angiogenesis in critical-defects within the calvarial region of mice (40) using multiphoton microscopy.

### *2.2.2 Widefield and confocal microscopy*

Widefield and confocal microscopy are similar imaging techniques which deliver fluorescent excitation light through on objective lens onto the target specimen (41). As previously mentioned, the main difference between these two techniques stems from the fact that



confocal microscopy uses a pinhole aperture where widefield does not. As such, widefield microscopy enables visualization of whole samples whereas confocal only allows image capture of a single focal spot at a time. This narrower field of view comes with the benefit of drastically increased spatial resolution, optical sectioning and image contrast. Laser confocal microscopy has been used to characterize electrospun fibrous membranes for bone defect repair (42). While not commonly employed in studying tissue defects, widefield microscopy has been used to image microvasculature in mice in order to monitor thrombus formation (43).

### *2.2.3 Intrinsic Optical Signaling, Multiphoton, OCT, and micro-CT*

Intrinsic optical signaling is an imaging technique that relies on a endogenous contrast mechanisms in native tissue to produce images that may be used to study morphological characteristics of vessels. As such, it can be used to visualize vascular networks without the need for dye administration, which requires an injection and may disrupt the normal blood flow patterns, and therefore the morphological observed characteristics. In biological systems, IOS is based on the differential absorption spectra of oxy- and deoxyhemoglobin (44). At an excitation wavelength of 573 nm, an isobestic point between oxygenated and deoxygenated hemoglobin can be observed. Therefore at 573 nm, since the absorption coefficients of oxygenated and deoxygenated hemoglobin are approximately equivalent, both components can be visualized together as total hemoglobin. Since hemoglobin is physiologically compartmentalized to the blood vessels, images acquired under 573 nm illumination make the blood vessels appear as dark structures against the grayscale background of the surrounding tissue. While IOS has been used to image the vascular networks in cerebral regions of mice and monkeys (45, 46), such techniques have not been used to observe vascular remodeling in bone defect sites.

Multiphoton microscopy is a fluorescence imaging technique that enables the imaging of live tissue up to a depth of approximately 1 mm (47). Multiphoton microscopes rely on “high-order nonlinear light-matter interactions, where multiple photons are required for contrast generation” (48) As such, the localization of excitation in photons results in greatly improved penetration depths and minimized photobleaching or photodamage to the specimen. Two-photon fluorescence is the most commonly employed multiphoton microscopy technique, however other

methods such as second harmonic generation, three-photon fluorescence, and even four-photon fluorescence do exist (48). Multiphoton microscopy is primarily used to visualize cells in immuno-oncology studies (47, 49) however it has recently been used to analyze tissue engineered scaffolds seeded with MSCs for diabetic wound healing (50) as well as angiogenesis in critical-sized defects of the calvarial region (51).

Optical Coherence Tomography is a well-studied imaging technique with applications ranging from animal studies to neurosurgical and tumor diagnostic tools (52). OCT utilizes the reflection of relatively low-wavelength light off biological tissue in a cross-sectional plane to produce high resolution images (53). Similar to multiphoton microscopy, OCT can be used for cellular and even subcellular level resolutions depending on the coherence length of light source used. OCT has also been used to map vascular networks in the cerebral regions of animal models (54, 55).

Micro-Computed Tomography is an x-ray transmission imaging technique that uses multiple 2D image slices to reconstruct a 3D visualization of the target specimen (56). It is a widely used technique in tissue engineering applications for its ability to image both blood vessels and bone structures on a micron scale.  $\mu$ CT has recently been used to image rhBMP-2 mediated segmental bone defect repair in murine models (57) as well as angiogenesis during bone regeneration in both non-critical (58) and critical-sized defects in the calvarial region of mice (59).

### **2.3 Monitoring Hemodynamic Response**

To determine the success of tissue engineering treatments in repairing orthopedic trauma is it important to evaluate not only the morphology of the newly regenerated vessels, but also their functionality. As such, complementary imaging modalities are needed in order to provide information on the hemodynamic response within defect sites. Commonly used methods that will be discussed in this section include laser speckle contrast (LSC) imaging, dynamic contrast enhanced-magnetic resonance imaging (DCE-MRI), and dynamic susceptibility contrast-magnetic resonance imaging (DSC-MRI). Additionally, we will discuss the administration of

vasodilators during the course of blood flow imaging in order to assess vascular maturity and compliance.

### *2.3.1 LSC, DCE-MR, and DSC-MR Imaging*

Laser speckle contrast imaging relies on the interference pattern that results when biological tissue is illuminated by a coherent light source (60). Tissue that contains blood vessels display particular interference patterns due to the movement of red blood cells through the vascular network. As such, blood vessels can be easily identified from the surrounding tissue, and the recorded interference or ‘speckle’ pattern integrated over a finite exposure time to produce maps of the relative blood flow values over the entire field of view (61, 62). LSC imaging has been previously used to monitor *in vivo* blood flow in cerebral (63) and retinal (64) areas in murine models. However, to the best of our knowledge it has not yet been used to map hemodynamic changes in tissue engineering applications.

DCE and DSC MRI are similar imaging techniques that require administration of a paramagnetic contrast agent in order to visualize hemodynamic responses in vascular networks. Gadolinium chelates are commonly used for both methods (65). DCE focuses on quantifying the permeability of blood vessels by measuring the leakage of the contrast dye from the vasculature using T1-weighted MRI, while DSC can be used to estimate vessel density and blood volume in the vascular network using T2 and T2\*-weighted MRI (66). These techniques are used to image perfusion in tumors (67), or in areas of the brain affected by strokes (68). However recently, DCE-MRI has also been employed to monitor angiogenesis in tissue engineering constructs for calvarial bone regeneration (69).

### *2.3.2 Administration of vasodilators to map vascular maturity and compliance*

Vasodilatory agents can cause vasodilation of blood vessels, resulting in increased blood flow and blood volume in the region of interest (70). Frequently used vasodilators in preclinical studies include prazosin, verapamil, cromakalim, and carbogen gas (71, 72). Regardless of the method chosen, the effect on the vascular network is similar. Each serves to slightly alter the pH

of the environment. This change in pH causes relaxation of the smooth muscle surrounding blood vessels, allowing them to dilate and prompting increased blood flow (73). Since smooth muscle takes time to develop around the newly formed vessels in a bone defect site, the administration of vasodilators can inform on the relative maturity of the blood vessels present.

## **2.4 Vascular tracer kinetics and stem cell tracking**

To further characterize vascular hemodynamics within an angiogenic vessel bed, alternative imaging modalities may be implemented. Fluorescence imaging is well suited for assessing the tracer kinetics of fluorescent dyes passing through vessel networks (74), while positron emission tomography (PET) may be used to create 3D reconstructed visualizations of nuclide tracers (75). Additionally, because cells can be fluorescently tagged, bleached, or transfected to display fluorescent proteins, fluorescence imaging can be used to track stem cells and monitor their differentiation (76, 77).

### *2.4.1 Fluorescence Imaging*

Fluorescence imaging is the visualization of fluorescent dyes or proteins and has a wide range of applications from guiding medical diagnostics (78) to measuring vascular characteristics (74). Fluorescence imaging has been previously utilized to assess the integration of tissue engineering grafts in mice (79) in addition to the tracking of induced pluripotent stem cells (76).

### *2.4.2 Positron emission tomography*

Positron emission tomography (PET) uses computer analysis to reconstruct images of gamma rays given off by positron emitting radionuclide tracers as they transit blood vessels in the target tissue (80). While often used for oncology diagnostic purposes (75), these 3D reconstructed maps have recently been used to analyze the stem cell mediated repair of segmental long-bone defects (81), and track human muscle precursor cells for the purpose of skeletal muscle tissue engineering (82).

## 2.5 Bone Visualization

In addition to imaging the morphological, hemodynamic, and tracer kinetic characteristics of vascular networks in bone defect sites, the volume of regenerated bone can also be used as a metric for treatment success. To determine the amount of regrown bone, several other imaging modalities including x-ray imaging, micro-computed tomography ( $\mu$ CT), MRI, and ultrasound imaging can be used. In this section, we will review each method's capabilities generating images of bone *in vivo*.

### 2.5.1 X-ray (radiography) and Micro-Computed Tomography

X-ray imaging is one of the oldest imaging techniques and uses electromagnetic radiation to produce 2D images of dense biological tissue. Electromagnetic waves are projected into the specimen and are absorbed by increasing amounts based on the density of the material they come into contact with. By placing a detector behind the specimen, any x-rays that pass through the specimen can be captured and used to produce images of the darker areas (e.g. bone) surrounded by less dense areas (e.g. blood and tissue) (83).  $\mu$ CT can be considered a direct advancement of x-ray imaging as this method uses the same principles but incorporates multiple 2D images at varying angles to produce a 3D reconstructed visualization of bone areas (56).  $\mu$ CT has been used in recent years to study bone formation around bioactive scaffolds in noncritical-sized defects within the mandibles of pigs (84), and to visualize bioactive glass foam scaffolds implanted into the legs of mice (56).

### 2.5.2 Ultrasound Imaging

Modern advancements in ultrasound techniques have enabled it to become a viable alternative to the traditional x-ray and  $\mu$ CT imaging of bone (85). Instead of monitoring the behavior of light or electromagnetic radiation when passing through biological tissue, ultrasound measures the absorbance and scattering of high frequency ( $\sim$ MHz) sound waves (86). The

specific type of ultrasound used to visualize bone is known as quantitative ultrasound and uses lower frequencies (4-10 MHz) which correlate to the density and composition of bone. As such, ultrasound has been used successfully to evaluate fracture healing in bone defects, even showing precise enough measurements to allow for the discrimination of distinct healing stages (86).

## CHAPTER 3: EXPERIMENTAL PROTOCOL AND IMAGING PROCESSING

### 3.1 3D scaffold fabrication

For the purpose of our tissue engineering experiments we created porous 3D-printed PCL scaffolds using a LulzBot TAZ printer with a 375  $\mu\text{m}$  diameter nozzle (Aleph Objectives, Inc.; Loveland, CO). Scaffold sheets with 0.5 mm thickness, 30% infill density, and rectilinear infill pattern were designed, sliced, and converted to G-code using Cura software (Ultimaker B.V.; Geldermalsen, Netherlands). PCL scaffold sheets were printed according to the G-code using an extrusion and cooling bed temperature of 105°C and 45°C, respectively. Cylindrical scaffolds were punched from the sheets using a 4 mm diameter drill bit. Prior to cell culture studies, cylindrical 3D-printed scaffolds were treated with 1 M NaOH for 1 h to increase surface hydrophilicity and washed 3 x 10 min in PBS. Scaffolds were then sterilized in 100% ethanol for 1 h, followed by 3 x 20 min washes in sterile PBS. One day prior to seeding, scaffolds were incubated in stromal medium (DMEM, 10% v/v FBS, 1% v/v P/S) at 37°C overnight to allow for serum proteins to adsorb to the scaffold surface.

### 3.2 Stem cell isolation and calvarial defect preparation

Lipoaspirate from a Caucasian female donor (39 y.o.) was obtained from Johns Hopkins Medical Institutions under an approved Institution Review Board protocol. To isolate adipose-derived stem cells (ASCs), lipoaspirate was digested with 1 mg/mL Collagenase I (Worthington Biochemical Corp.; Lakewood, NJ) at 37°C for 1 h and centrifuged at 300 g for 10 min to obtain a pellet of stromal vascular fraction. Following cell resuspension, RBCs were removed by lysing RBCs in a buffer (155 mM  $\text{NH}_4\text{Cl}$ , 10 mM  $\text{KHCO}_3$  and 1 mM EDTA) for 7 min and centrifuging at 300 g for 5 min. The stromal vascular fraction pellet was resuspended and plated onto T-175 flasks to allow for expansion of the adherent ASC population. ASCs were expanded using expansion medium (DMEM, 10% v/v FBS, 1% v/v P/S, 1 ng/mL FGF-2) for two passages (P2) before use in experiments.

3D-printed scaffolds were then seeded with ASCs encapsulated within a fibrin gel as previously described (87). P2 ASCs were trypsinized and resuspended in 10 mg/mL fibrinogen at a density of  $25 \times 10^6$  cells/mL. Thrombin (10 units/mL) was added to the ASC-fibrinogen mixture (1:4 v/v) to yield a cell concentration of  $20 \times 10^6$  cells/mL, and 6  $\mu$ L of the solution was infused into the pore spaces of 3D-printed scaffolds. Scaffolds were incubated at 37°C for 30 min to allow for fibrin to completely crosslink prior to adding culture medium. Scaffolds were incubated in stromal medium overnight prior to *in vivo* implantation.

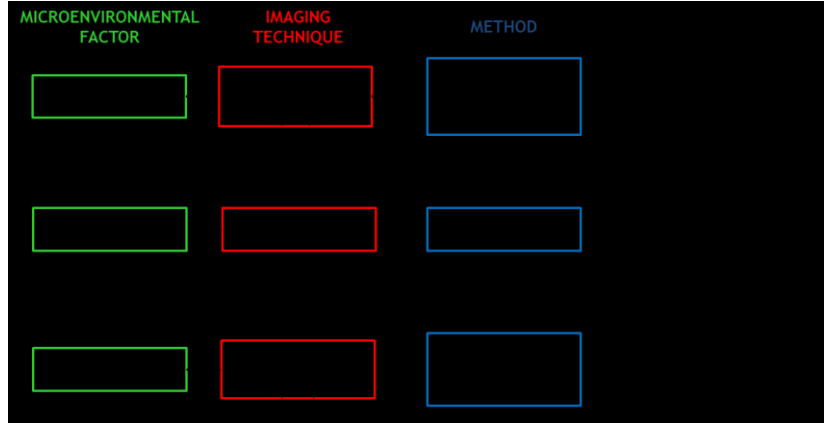
All animal procedures were approved by the Johns Hopkins Animal Care and Use Committee (JHU ACUC). Male 11-week-old homozygous Nu/J mice (Jackson Laboratories; Bar Harbor, ME) were anesthetized using isoflurane and injected subcutaneously with 0.2 mg/kg buprenorphine (Reckitt Benckiser Pharmaceuticals, Inc.; Slough, UK) prior to surgery. After sterilizing skin at the surgical site with betadine, an incision was made to expose the calvarium, and the pericranium was gently removed to allow for drilling of the defect. A 4-mm diameter defect was drilled in the right calvarium using an Ideal Micro-Drill (Harvard Apparatus; Holliston, MA) and 4 mm circular knife (Xemax Surgical Products, Inc.; Napa, CA). Special care was taken to avoid disrupting the underlying dura mater. Scaffolds were implanted by briefly washing them in sterile 0.9% NaCl and press-fitting them into the defect. The incision was then sutured using 6-0 nylon sutures to close the surgical wound. Animals were treated with an intraperitoneal injection of 0.2 mg/kg buprenorphine twice a day for 2 days following surgery for pain management.

### **3.3 Multimodal Imaging Acquisition**

To image microvascular structure and function in the scaffold and tissue microenvironment, we used a minimally invasive multicontrast optical imaging setup. This imaging system acquires high temporal (10 fps) and spatial resolution (5  $\mu$ m) images, and is capable of three imaging modalities: intrinsic optical signal (IOS), laser speckle contrast (LSC) and fluorescence (FL) imaging. . **Fig. 2** summarizes the microenvironmental parameters obtained from the three imaging techniques used.



We used a white light source (NI-150, Nikon Instruments Inc., NY) coupled with two band-pass filters (560 and 570±5nm) to provide illumination for IOS imaging along with a filter wheel



(FW102C, Thorlabs,NJ). A 632.8 nm HeNe laser (0.5mW, Thorlabs, NJ) was used to acquire LSC images, and a 473 nm laser (100mW, Cobalt

**Fig. 2: Multi-contrast in vivo imaging of the graft microenvironment.** Flow chart illustrating key microenvironmental factors that are interrogated in vivo (green) within the calvarial defect site; the in vivo optical contrast mechanism employed (red) to assay these factors; the imaging method employed (blue), and the metrics computed for characterizing the in vivo graft microenvironment. \* Can also be used to track fluorescently labeled stem cell survival and location.

AB, Sweden) along with a 496 nm long-pass filter (FF01-496/LP-25, Semrock Inc.,NY) was used for acquiring fluorescence images. Mice were first anesthetized using a controlled flow rate of 1.5% isoflurane (Iso Flo, Cat. No. 06-8550-2/R1) in 1L/min air with a Vapomatic Model: 2 (AM Bickford Inc., NY) before being placed on an adjustable platform with their heads secured in place using a custom designed stereotaxic frame. A multi-lens set (AF Micro Nikkor 60mm 1:2:8D, Nikon Instruments Inc., NY) was used for image acquisition at 0.5 magnification using a CCD camera (Infinity 3, Lumenera, ON, Canada) controlled by a customized MATLAB® (MathWorks; Natick, MA) program. IOS images were used to characterize *in vivo* changes in microvascular morphology and fluorescence images were used to detect RFP-tagged cells and intravascular FITC conjugated dextran (70 kD). Lastly, we employed LSC imaging for analyzing perfusion changes and microvessel maturity within the scaffold microenvironment.

### 3.3.1 IOS

For IOS, the governing equation was developed from a modified version of the Beer-Lambert's Law (44) as shown in **Eq. 1**. Here the logarithmic ratio of the incident light ( $I_o$ ) and the reflected light ( $I_r$ ) divided by the length traveled by the light ( $L$ ) is equal to the absorption coefficient ( $\mu$ ) multiplied by the concentration of both oxygenated and deoxygenated hemoglobin.

$$\frac{\ln\left(\frac{I_o(\gamma)}{I_\alpha(\gamma)}\right)}{L(\gamma)} = \mu_{HbO}(\gamma) \cdot [HbO] + \mu_{Hb}(\gamma) \cdot [Hb] \quad (1)$$

At the isobestic point of 570nm, where the absorption coefficients of oxygenated and deoxygenated hemoglobin are approximately equal, one can reduce **Eq. 1** to **Eq. 2**.

$$\ln(I_o) - \ln(I_\alpha) \propto HbT \quad (2)$$

Therefore, if we consider background pixels within our image to be points where nearly all light is reflected then the images we capture show background tissue as bright since they lack hemoglobin and blood vessels appear dark, since they are hemoglobin rich structures. For our experiments, IOS images were acquired at 10 fps with an exposure time of 60 ms.

### 3.3.2 FL

For FL tracer experiments, 0.2 mL of 10 mg/mL 70 kD dextran-FITC was administered through a tail-vein injection. The transit of FITC through the microvascular bed at the graft site was then imaged under blue laser (i.e. 473 nm) illumination at 10 fps with an exposure time of 150 ms for ~3 min.

### 3.3.3 LSCI

For LSC, speckle fluctuations or the degree of ‘blurring’ was quantified using **Eq. 3** (88). Acquiring a temporal stack of the speckle pattern with a CCD camera over a given exposure time allows us to quantify the degree of blurring, which is inversely proportional to the relative perfusion. Each pixel in our FoV was assigned a speckle contrast or  $K$  value, which was the ratio of the standard deviation,  $\sigma$ , to the mean pixel intensity,  $\langle I \rangle$ , where  $K^2$  is inversely proportional to the moving object’s flow velocity. For each pixel, a moving average was calculated in order to obtain a smoothed image.

$$K = \frac{\sigma}{\langle I \rangle}, K^2 \propto \frac{1}{v} \quad (3)$$

The variance of the time-averaged pixel intensity was equal to its temporal fluctuations and is given by **Eq. 4**, below (62). Here,  $T$  is the camera exposure time,  $c_\tau$  is the temporal average of the intensity autocorrelation function, and  $\tau$  is the decorrelation time.

$$\sigma^2 = \frac{1}{T} \int_0^T c_\tau(\tau) d\tau \quad (4)$$

Using LSC, we also employed a carbogen gas challenge to assess the *in vivo* hemodynamic response and map vessel maturity. Carbogen gas, a mixture of 95% oxygen and 5% carbon dioxide, increases cerebral blood flow via vasodilation (71). At a microvascular level, increased oxygen delivery causes changes in tissue perfusion, which alters vascular resistance and perfusion pressure (89). Carbon dioxide causes a decrease in pH within the blood which is detected by receptors in the vessels walls that then cause the vessel smooth muscle to relax, resulting in vasodilation (90). In our protocol, mice were administered alternate cycles of room air and carbogen gas in 3 minute and 30 second blocks respectively, and LSC image stacks were acquired during the entire experiment. The raw speckle data was smoothed using a 10×10 pixel median filter, and a 3×3 pixel temporal Gaussian filter to reduce noise and increase the signal to noise ratio (SNR) of the LSC images. Images were acquired at 10 fps with an exposure time of 60 ms.

### 3.4 Image Processing Methods

Prior to analyzing our acquired image stacks, a number of resampling, registration, smoothing, filtering, and thresholding steps were required. In this way, we were able to generate clear ‘vessel masks’ which could then be used to study the vascular morphology, tracer kinetics, and hemodynamics of our newly regenerated vessel beds.

#### 3.4.1 Resampling Fixed Time Points and Image Registration

For processing of FL images, the acquired image stack was first imported into MATLAB® and resampled using linear interpolation to create image stacks with 50 ms temporal resolution. After acquiring image stacks using IOS, LSC, and FL imaging, image processing was performed using ImageJ (91) and MATLAB®. Image stacks from each imaging modality were co-registered

using the ImageJ plugin TurboReg (92). This allowed us to directly compare microvascular parameters across each modality.

#### *3.4.2 Smoothing, Gaussian, and Low-Pass Filters*

For IOS and LSC images, maximum intensity projection (MIP) images of each image stack were generated and corrected for non-uniform illumination using a rolling ball background subtraction of 50 pixels in radius. FL image stacks were subjected to a low pass filter at a cutoff frequency of 1 Hz to remove ‘spot’ noise

#### *3.4.3 Gaussian and Hessian Filter for distinguishing vessels*

Next, blood vessels were segmented using an ImageJ plugin called a ‘tubeness’ filter that distinguishes curvilinear or tubular structures such as blood vessels, bronchi or neurons by computing the 3D Hessian (93). The plugin employs Gaussian convolution with standard deviation,  $\sigma$ , which we varied to segment blood vessels of different radii. We selected three  $\sigma$  values ranging from 0.5-3 for each IOS MIP image in order to segment every vessel. Subsequently, IOS output images from the tubeness filter were combined using a ‘maximum’ operator while LSCI output images were combined using an average intensity projection of the baseline blood flow stack. This step was necessary to preserve blood vessel morphology because blood vessels dilated during administration of the carbogen gas.

#### *3.4.4 Thresholding and Particle Filtration*

After producing maximum and average intensity projections of our image stacks, these output images were thresholded to yield binary ‘vessel masks’. Next, morphological operations such as image opening and closing were used to restore portions of blood vessels lost during the thresholding step. Finally, any residual noise outside the graft area was removed using a minimum size filter of 10 square pixels to yield the final blood vessel masks. Finally, the IOS and LSC derived blood vessel masks were combined to yield an overall mask that allowed us to accurately analyze the morphology of the microvasculature within the field of view.

### *3.4.5 Euclidean Distance Maps and Tagged Skeletons*

Next, we generated a tagged skeleton and a Euclidean distance map (EDM) of the overall blood vessel mask using ImageJ. A tagged skeleton is an image wherein the morphology of the segmented blood vessels is represented as single pixel-wide branches along their centerline. These pixels were then classified based on the number of connected neighbors as ‘end points’ or ‘junctions’ (94). The tagged skeleton image can therefore be used to identify branch points in the microvascular tree, the total number of vessels present, and assess vessel length. The Euclidean distance map computed from our overall vessel mask replaces background pixels with grayscale values corresponding to their distance from the nearest blood vessel boundary (95). Therefore, when logically combined with the tagged skeleton, the EDM can be used to represent the average radii of all vessel segments in the overall blood vessel mask. This approach yields maps of the blood vessels within the graft site coded by their morphological parameters (i.e. vessel radii, vessel length, and tortuosity) and depict valuable information that can be used to quantify angiogenesis at the graft site.

To assess the relative blood flow within the vessels permeating our scaffold, we began by using the aforementioned methods for determining and mapping vessels within the overall mask. Next, we created average intensity projection images from the baseline blood flow (i.e. LSC) time series over 12 min, as well as the blood flow time series during carbogen gas experiments (i.e. three cycles of air for 3.5, 5.5, and 4.5 min interspersed with two cycles of carbogen gas inhalation for 1 min). By utilizing the vessel segment information from the tagged skeleton image, the blood vessel dimensions from EDM images and computing the grayscale pixel intensity from the average projection images, we were able to map the relative blood flow per vessel segment. In order to more easily compare the baseline and carbogen blood flow values, we normalized these data by dividing the grayscale intensity values assigned to each vessel segment by the maximum value that occurred across all LSC trials during the carbogen inhalation experiment, resulting in a relative blood flow value scaled between 0 and 1. To assess the change in blood flow in response to carbogen gas inhalation, the percent increase in the

average pixel intensity per vessel segment between baseline air and carbogen inhalation states was computed and mapped to the overall vessel mask. By quantifying carbogen gas-induced changes in blood flow we could quantify the relative maturity of each vessel segment within the angiogenic graft site. These changes correspond to fluctuations in blood flow caused by vasodilation in mature blood vessels.

## CHAPTER 4: ANALYZING VASCULAR REMODELING DATA

After processing out images and creating vessel masks, we used a k-means clustering approach implemented in MATLAB® to classify each vessel segment based on its change in blood flow during carbogen gas inhalation. The input to the k-means clustering was an array containing the flow values of each vessel segment and the output was a list of four classes that partitioned these flow values based on their nearest means. The index values allocated to these classes were then mapped to the corresponding vessels.

### 4.1 Results

Using IOS and LSC images of the calvarial defect site (**Fig. 3a, b**) we generated binary vessel masks derived from each modality (**Fig. 3c, d**), which were combined to create an overall mask (**Fig. 3e**) that was used to analyze all morphological parameters. With the tagged skeleton

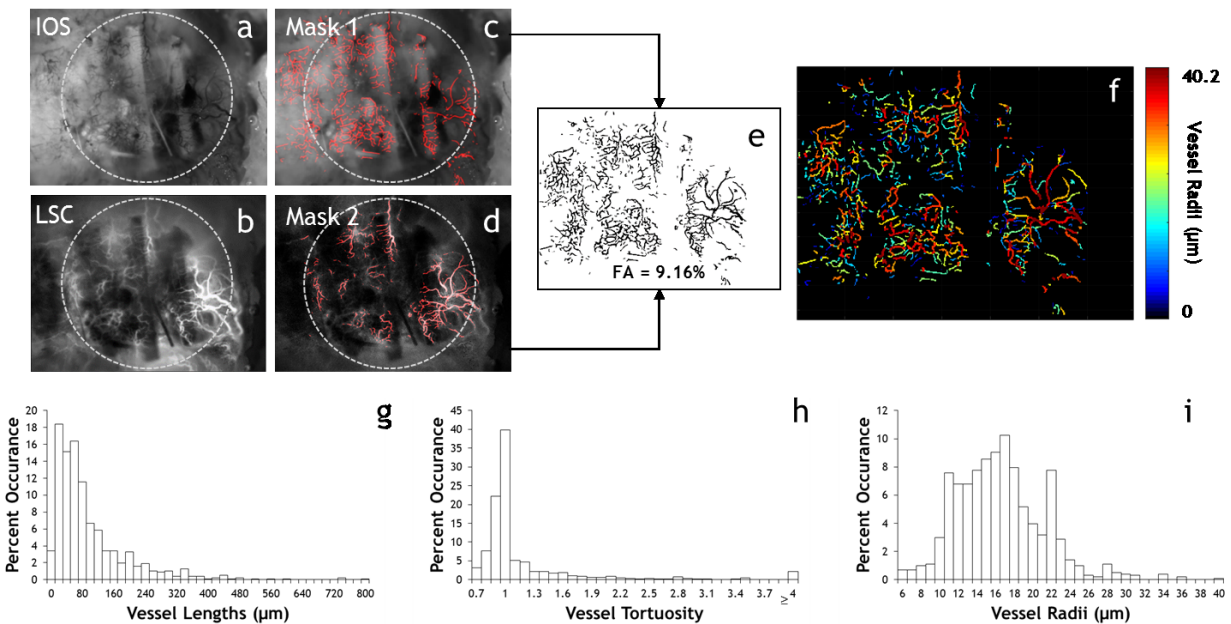


**Fig. 3: Analysis of vascular morphology in the in vivo graft microenvironment.** (a) IOS image of the calvarial defect site two weeks after implantation wherein the vasculature is dark due to green light absorption. PCL scaffold is outlined by the gray circle. (b) LSC image of the same FoV wherein perfused blood vessels appear bright due to red laser light being scattered by moving erythrocytes. PCL scaffold is again outlined by a gray circle. (c, d) Images in (a, b) overlaid with their respective binary vessel masks. (e) Combination of the vessel masks in (c, d) to provide a holistic mask of all the vessels that are visible using either imaging method. (f) Map of the average vessel radius corresponding to the vessel segments identified in (e). (g, h, i) Distribution of vessel characteristics for the sample shown in (e).

and EDM derived from the overall mask we were able to visually represent characteristics of the vascular network as shown in **Fig. 3f**. Here we can see that there was a wide range of vessel radii distributions within the scaffold site. The minimum measurable radius was 5.6  $\mu\text{m}$  due to the resolution of the camera sensor and optics. **Fig. 3g**, **Fig. 3h**, and **Fig. 3i** show the distributions of vessel characteristics assessed from the overall vessel mask (**Fig. 3e**). For the distribution shown in **Fig. 3g** the average vessel length was 93.4  $\mu\text{m}$  with the most frequently occurring bin falling between 20-40  $\mu\text{m}$  and a maximum vessel length of 793.1  $\mu\text{m}$ . Similarly, from **Fig. 3h** we see the most frequent range of vessel tortuosities was between 0.7-1 with an average of 1.22 and a maximum  $\geq 4$ . Additionally from **Fig. 3i**, the most frequent range of vessel radii was from 16-17  $\mu\text{m}$  with an average of 16.6  $\mu\text{m}$  and a maximum of 40.2  $\mu\text{m}$  which matched the values displayed in the vessel map (**Fig 3f**). This morphological data regarding the blood vessels within the graft site provides invaluable information regarding angiogenesis within the scaffold. Furthermore, these measurements can be used to characterize the vessel phenotypes as described in the *Discussion*.

From the image stacks of the dextran-FITC injections obtained using FL imaging we were able to clearly observe the transit of the tracer through the vascular bed (**Fig. 4a**) within the graft site. To illustrate the first-pass of dextran-FITC through the microvasculature, we plotted the mean fluorescent signal intensity of from a sub-region (**Fig. 4b**) wherein one can clearly observe the wash-in and wash-out of the tracer and the contribution of individual time points to the overall tracer curve. By importing the image sequence into MATLAB we could determine the time-to-peak value per vessel segment and map these values to our overall vessel mask (**Fig. 4c**). Finally, using FL imaging we were also able to capture the distribution of HUVEC tagged with RFP within the scaffold (**Fig. 4d**).



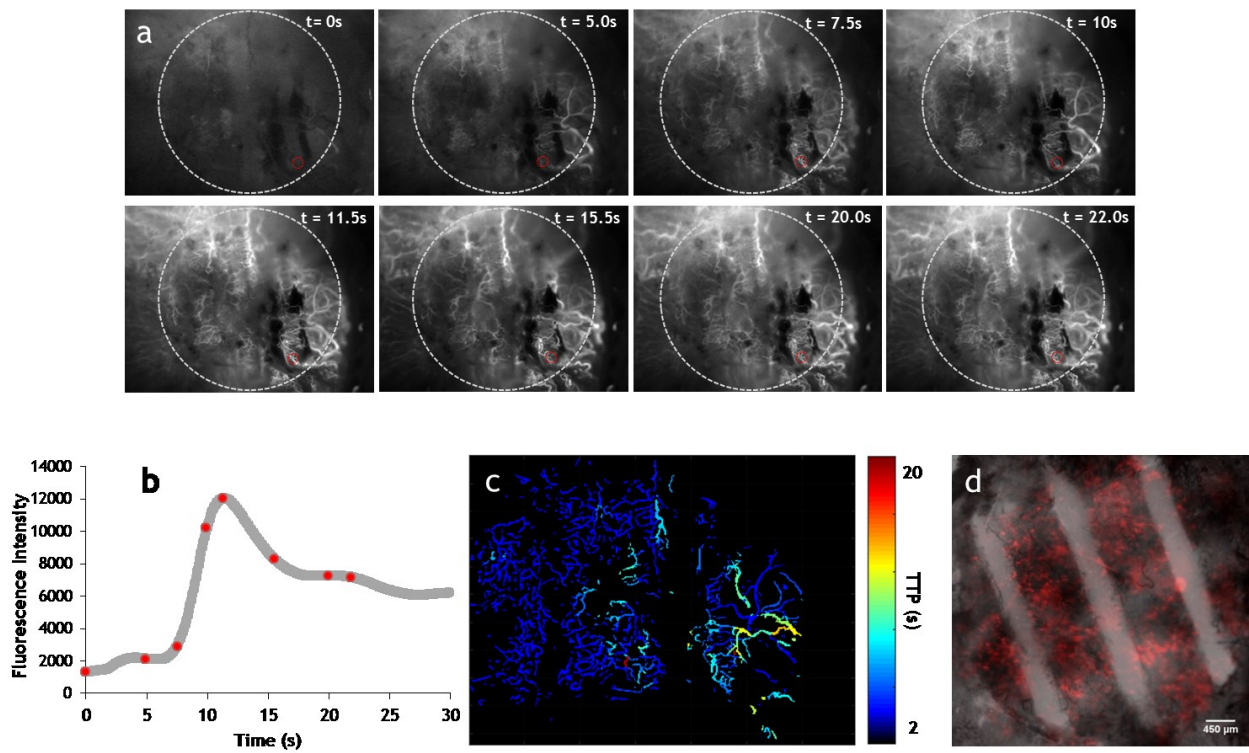


**Fig. 4: Analysis of tracer kinetics and cell distribution in the in vivo graft microenvironment.** (a) Representative time series of fluorescent images acquired after injection of the fluorescent intravascular tracer FITC-dextran. PCL scaffold is outlined by the large gray dashed circles.(b) Plot of the fluorescence intensity from the ROI (red circle) in (a) illustrating the transit of the intravascular tracer through the vasculature within the graft. Red points correspond to the time points for which snapshots are shown in (a). (c) Time-to-peak (TTP) map computed from the tracer data for each vessel segment within the FoV. (d) Fluorescent image of a scaffold seeded with a mixture of ASCs and red fluorescent protein (RFP) labeled HUVECs (red channel) illustrating the utility of the fluorescent channel for cell tracking.

From the overall vessel mask and the average intensity projections during air and carbogen breathing blocks, we were able to map changes in blood flow within the microvascular network at the graft site (**Fig. 5a, b**). In order to compare measurements, these values were normalized to the highest recorded blood flow value across all experiments. Using these normalized blood flow maps, we calculated the percent change in blood flow due to carbogen inhalation (**Fig. 5c**). Blood flow changes as high as 25% were observed in some vessels. In order to more closely analyze the blood flow response, we plotted the percent change in blood flow for a single vessel (**Fig. 5d**) over the course of the carbogen inhalation experiment as shown in **Fig. 5e**. Here we can see that blood flow in the target vessel responded clearly and consistently during the carbogen inhalation blocks. Finally, using a k-means clustering approach we classified each blood vessel based its magnitude of blood flow change (**Fig. 5f, g**) and then applied the same cluster class to additional vessel characteristics in order to ascertain the relationship between parameters such as vessel radii or TTP and the observed change in blood flow. As shown in **Figs.**

5h and 5i, vessel radius did not correlate with the blood flow response, while the TTP in vessels tended to be longer for vessels that exhibited larger blood flow changes within the graft site.

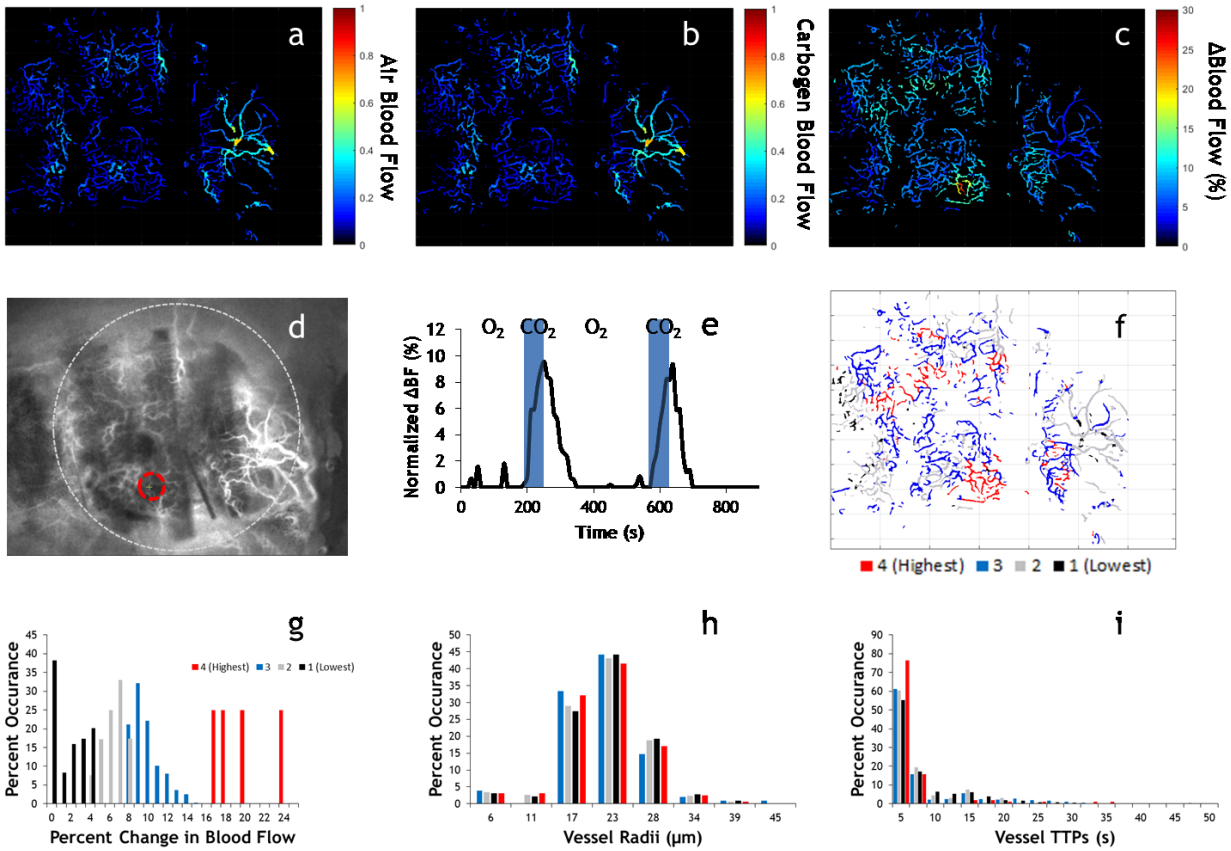


**Figure 5: Analysis of perfusion and vessel maturity in the in vivo graft microenvironment.** (a) Baseline blood flow map (normalized to the maximum flow across all samples). (b) Normalized blood flow map generated by computing the average blood flow during the carbogen inhalation periods. (c) Map of the percent change in blood flow induced by carbogen inhalation. More mature blood vessels exhibit larger changes in blood flow. Note only positive changes are displayed. (d) LSC image indicating ROI (red circle) corresponding to the blood flow time course in (e). PCL scaffold is outlined by gray circle. Time series were baseline corrected and only positive perfusion changes were plotted. The robust response to carbogen inhalation in (e) during the 240-300 s (blue bar) and 540-600 s (blue bar) intervals indicate the degree of maturity of the blood vessels within the red circle in (d). (f) Vessel classification of carbogen response in (c) using k means clustering. Vessels appearing as red are those that indicated the greatest degree in blood flow change while black indicates the lowest change. (g) Probability distribution function of change in blood flow in response to carbogen as seen in (f). (h) Probability distribution function of vessel radii according to the same classifications in (g) and (f). The lack in variability across vessel sizes indicates that radius had no effect on carbogen response. (i) Similar distribution as seen in (h) but with the time to peak of each vessel. Again, the lack in variability indicates a lack of a relationship between carbogen response and time to peak response following injection of the dextran-FITC tracer.

## 4.2 Discussion

Achieving adequate vascularization in tissue engineered bone grafts is critical to their engraftment, long term survival and eventual clinical success. It is well known that blood vessels are essential for graft survival because they deliver O<sub>2</sub> and essential nutrients, while also removing cellular waste products. However, vasculature is also essential for bone development and homeostasis, with several studies demonstrating that the coupling of angiogenesis and osteogenesis is necessary for bone growth and remodeling (96, 97). Additionally, the blood vessel phenotype plays a critical role in this process. For example, vessels that contribute to bone growth – termed “Type H vessels” – exhibit higher blood flow, CD31 and endomucin expression, and secretion of pro-osteogenic factors (97, 98), and have a thinner, more elongated morphology than other bone vessels (8). Furthermore, osteoprogenitors and osteoblasts are intimately associated with Type H vessels, typically residing within 20 μm of the nearest vessel (96). In light of these findings, some investigation into blood vessel phenotypes within implanted tissue engineering bone grafts has been performed (99). However, most current tissue engineering approaches do not utilize imaging techniques capable of adequately assessing the role of the vascular phenotype and angiogenic-osteogenic coupling in bone regeneration.

Herein lies the value of our imaging system, which combines IOS, LSC, and FL imaging in a way that enables the robust characterization of the vasculature in tissue engineered bone grafts *in vivo*. Since our system was designed to specifically image microvascular networks *in vivo*, it avoids the disadvantages of tissue clearing approaches used for ex vivo imaging such as distortion of the microvascular architecture and a lack of blood flow information (37).

Blood vessel maturity can be estimated by quantifying the degree to which blood vessels respond to a vasodilatory challenge, such as carbogen gas inhalation. The underlying premise being that this blood flow response is proportional to the degree of smooth muscle coverage that has developed around blood vessels at the graft site. Here, we chose to evaluate vessel maturity by measuring the blood flow responses during carbogen challenges with LSC imaging because it is less sensitive to inaccuracies such as motion within the FoV. Although one could derive such estimates from IOS imaging by determining changes in microvessel diameter induced by carbogen, such measurements are challenging since small changes in blood vessel diameter are

susceptible to noise resulting from subject motion. LSC imaging is not without its own drawbacks however, as it is difficult to determine whether blood vessels within the graft site are themselves responding to the carbogen or if the increased blood flow is the result of upstream vasodilation. Additionally, while LSCI does provide valuable information on the relative blood flow changes, an imaging method that permits absolute blood flow measurements would be preferable for certain applications.

By permitting the evaluation of parameters such as vascular morphology, blood flow, and blood vessel maturity, our imaging system facilitates the characterization of the vascular phenotype. Combining this multimodal imaging platform with clustering and structural/functional blood vessel mapping enables us to quantify changes that accompany the developing or angiogenic vascular bed within a tissue engineered scaffold. Such observations are critical for accurately assessing the regenerative potential of bioactive scaffolds as well as for informing their design. Future applications of this imaging platform involve its use to understand the effect of vessel phenotypes on the regenerative microenvironment within the graft. Furthermore, quantitative comparison of these vascular phenotypes across various tissue engineered scaffolds would enable us to better understand the success or limitations of different approaches for treating critical size calvarial defects. Finally, by tracking the location of implanted stem cells relative to the angiogenic blood vessels, one could follow their differentiation and impact on bone reformation.

## CHAPTER 5: CONCLUSIONS AND FUTURE RESEARCH

In this thesis, we have reviewed the previously used bone grafts techniques used to treat orthopedic defects, their shortcomings, and novel approaches to improve upon defect treatment using tissue engineering methods. Additionally, we have reviewed an extensive list of imaging techniques that may be used to characterize defect sites either through visualization of bone or the angiogenic network during wound healing. Finally, we have described a novel multimodal system for imaging the microenvironment of bioactive scaffolds for tissue engineering applications *in vivo*. Our system facilitates the use of IOS, FL, and LSC imaging during a single experimental session in order to provide extensive data on the regrowth of the vascular network and characterization of the vascular phenotypes involved in bone healing. IOS imaging allows us to assess changes in vascular morphology, while FL imaging enables tracking of cell distribution within the scaffolds as well as measurement of tracer kinetic phenomena. LSC imaging provides crucial information on relative blood flow and vessel maturity within a vascular bed that is being dynamically remodeled during osteogenesis. Finally, the multimodal imaging in conjunction with the analyses methods described here make it possible to compare angiogenesis within defect sites across different experimental paradigms. We believe that such tools provide critical information to help optimize the design, implementation and deployment of future tissue engineering approaches for critical sized calvarial defects.

Future experiments should therefore seek to improve upon the healing capabilities of tissue engineering scaffolds by studying the types and compositions of osteogenic and biochemical factors that best facilitate bone and vascular remodeling. In order to further study the characteristics associated with improved regeneration using our imaging system and processing techniques, more animals should also be imaged. In this way, we may achieve a better understanding of important vessel characteristics through a k-means clustering analysis with a more suitable population size.

## CHAPTER 6: BIBLIOGRAPHY

1. Dong C, Lv Y. Application of Collagen Scaffold in Tissue Engineering: Recent Advances and New Perspectives. *Polymers* (20734360). 2016;8(2):1.
2. Fahy N, Alini M, Stoddart MJ. Mechanical stimulation of mesenchymal stem cells: Implications for cartilage tissue engineering. *Journal of Orthopaedic Research*. 2018;36(1):52.
3. Jiang J, Fan CY, Zeng BF. Experimental construction of BMP2 and VEGF gene modified tissue engineering bone in vitro. *International Journal Of Molecular Sciences*. 2011;12(3):1744.
4. Albrektsson T, Johansson C. Osteoinduction, osteoconduction and osseointegration. *European Spine Journal: Official Publication Of The European Spine Society, The European Spinal Deformity Society, And The European Section Of The Cervical Spine Research Society*. 2001;10 Suppl 2:S96.
5. Oryan A, Alidadi S, Moshiri A, Maffulli N. Bone regenerative medicine: classic options, novel strategies, and future directions. *Journal of Orthopaedic Surgery & Research*. 2014;9(1):1.
6. Manassero M, Viateau V, Matthys R, Deschepper M, Vallefucio R, Bensidhoum M, et al. A novel murine femoral segmental critical-sized defect model stabilized by plate osteosynthesis for bone tissue engineering purposes. *Tissue Engineering. Part C, Methods*. 2013;19(4):271.
7. Jin Q, Giannobile WV. SDF-1 Enhances Wound Healing of Critical-Sized Calvarial Defects beyond Self-Repair Capacity. *PLoS ONE*. 2014;9(5):1.
8. Bixel MG, Kusumbe AP, Ramasamy SK, Sivaraj KK, Butz S, Vestweber D, et al. Flow Dynamics and HSPC Homing in Bone Marrow Microvessels. *Cell reports*. 2017;18(7):1804-16.
9. Lo Celso C, Fleming HE, Wu JW, Zhao CX, Miake-Lye S, Fujisaki J, et al. Live-animal tracking of individual haematopoietic stem/progenitor cells in their niche. *Nature*. 2009;457(7225):92-6.
10. Joon YL, Musgrave D, Pelinkovic D, Fukushima K, Cummins J, Usas A, et al. Effect of Bone Morphogenetic Protein-2-Expressing Muscle-Derived Cells on Healing of Critical-Sized Bone Defects in Mice. *Journal of Bone & Joint Surgery, American Volume*. 2001;83(7):1032.

11. Tarchala M, Engel V, Harvey EJ, Barralet J. A pilot study: Alternative biomaterials in critical sized bone defect treatment. *Injury*. 2018;49(3):523.
12. F2721 Standard Guide for Pre-clinical in vivo Evaluation in Critical Size Segmental Bone Defects. 2008 Nov 1,.
13. Bruder SP, Kraus KH, Goldberg VM, Kadiyala S. The effect of implants loaded with autologous mesenchymal stem cells on the healing of canine segmental bone defects. *The Journal Of Bone And Joint Surgery.American Volume*. 1998;80(7):985.
14. Cook SD, Salkeld SL, Brinker MR, Wolfe MW, Rueger DC. Use of an osteoinductive biomaterial (rhOP-1) in healing large segmental bone defects. *J Orthop Trauma*. 1998;12(6):407.
15. Strub M, Van Bellinghen X, Fioretti F, Bornert F, Benkirane-Jessel N, Idoux-Gillet Y, et al. Maxillary Bone Regeneration Based on Nanoreservoirs Functionalized e-Polycaprolactone Biomembranes in a Mouse Model of Jaw Bone Lesion. *BioMed Research International*. 2018:1.
16. Tubbs RS, Bosmia AN, Cohen-Gadol AA. The human calvaria: a review of embryology, anatomy, pathology, and molecular development. *Child's Nervous System: Chns: Official Journal Of The International Society For Pediatric Neurosurgery*. 2012;28(1):23.
17. Samsonraj RM, Dudakovic A, Zan P, Pichurin O, Cool SM, van Wijnen AJ. A Versatile Protocol for Studying Calvarial Bone Defect Healing in a Mouse Model. *Tissue Engineering.Part C, Methods*. 2017;23(11):686.
18. Stavropoulos A, Sculean A, Bosshardt DD, Buser D, Klinge B. Pre-clinical in vivo models for the screening of bone biomaterials for oral/craniofacial indications: focus on small-animal models. *Periodontol 2000*. 2015;68(1):55-65.
19. Liu C, Castillo AB. Targeting Osteogenesis-Angiogenesis Coupling for Bone Repair. *J Am Acad Orthop Surg*. 2018;26(7):e153.
20. Schipani E, Maes C, Carmeliet G, Semenza GL. Regulation of Osteogenesis-Angiogenesis Coupling by HIFs and VEGF. *Journal of Bone & Mineral Research*. 2009;24(8):1347.

21. Street J , Lenehan B. Vascular endothelial growth factor regulates osteoblast survival - evidence for an autocrine feedback mechanism. *Journal of Orthopaedic Surgery & Research*. 2009;4:19.
22. Kusumbe AP, Ramasamy SK, Adams RH. Coupling of angiogenesis and osteogenesis by a specific vessel subtype in bone. *Nature*. 2014;507(7492):323.
23. Prentice DA. Adult Stem Cells. *Issues Law Med*. 2004;19(3):265.
24. PIORE A. Stem Cells. *Discover*. 2016;37(6):42.
25. Tao H, Chen X, Wei A, Song X, Wang W, Liang L, et al. Comparison of Teratoma Formation between Embryonic Stem Cells and Parthenogenetic Embryonic Stem Cells by Molecular Imaging. *Stem Cells International*. 2018:1.
26. Park HJ, Zhang Y, Georgescu SP, Johnson KL, Kong D, Galper JB. Human umbilical vein endothelial cells and human dermal microvascular endothelial cells offer new insights into the relationship between lipid metabolism and angiogenesis. *Stem Cell Reviews*. 2006;2(2):93.
27. Wang Y, Liu JA, Leung KKH, Sham MH, Chan D, Cheah KSE, et al. Reprogramming of Mouse Calvarial Osteoblasts into Induced Pluripotent Stem Cells. *Stem Cells International*. 2018:1.
28. Abdallah BM. Marrow adipocytes inhibit the differentiation of mesenchymal stem cells into osteoblasts via suppressing BMP-signaling. *J Biomed Sci*. 2017;24(1):11.
29. Liao J, Wei Q, Zou Y, Fan J, Song D, Cui J, et al. Notch Signaling Augments BMP9-Induced Bone Formation by Promoting the Osteogenesis-Angiogenesis Coupling Process in Mesenchymal Stem Cells (MSCs). *Cellular Physiology And Biochemistry: International Journal Of Experimental Cellular Physiology, Biochemistry, And Pharmacology*. 2017;41(5):1905.
30. Jae-Yong Tae, Sung-II Lee, Ko Y, Jun-Beom Park. The use of adipose-derived stem cells for the fabrication of three-dimensional spheroids for the osteogenic differentiation. *Biomedical Research (0970-938X)*. 2017;28(16):7098.



31. Campana V, Milano G, Pagano E, Barba M, Cicione C, Salonna G, et al. Bone substitutes in orthopaedic surgery: from basic science to clinical practice. *J Mater Sci Mater Med*. 2014;25(10):2445.
32. Crostelli M, Mazza O, Mariani M, Mascello D, Iorio C. Adolescent idiopathic scoliosis correction by instrumented vertebral arthrodesis with autologous bone graft from local harvesting without bone substitute use: results with mean 3 year follow-up. *European Spine Journal: Official Publication Of The European Spine Society, The European Spinal Deformity Society, And The European Section Of The Cervical Spine Research Society*. 2018.
33. FerrettiCarlo, Muthray E, Rikhotso E, Reyneke J, Ripamonti U. Reconstruction of 56 mandibular defects with autologous compressed particulate corticocancellous bone grafts. *British Journal of Oral and Maxillofacial Surgery*. 2016;54(3):322.
34. Studwell AJ, Kotton DN. A shift from cell cultures to creatures: in vivo imaging of small animals in experimental regenerative medicine. *Molecular Therapy: The Journal Of The American Society Of Gene Therapy*. 2011;19(11):1933.
35. Ong SL, Gravante G, Metcalfe MS, Dennison AR. History, ethics, advantages and limitations of experimental models for hepatic ablation. *World Journal Of Gastroenterology*. 2013;19(2):147.
36. Moleiro AF, Concei G, Leite-Moreira A, Rocha-Sousa A. A Critical Analysis of the Available In Vitro and Ex Vivo Methods to Study Retinal Angiogenesis. *Journal of Ophthalmology*. 2017:1.
37. Steinman J, Koletar MM, Stefanovic B, Sled JG. 3D morphological analysis of the mouse cerebral vasculature: Comparison of in vivo and ex vivo methods. *PLoS ONE*. 2017;12(10):1.
38. Conchello J, Lichtman JW. Optical sectioning microscopy. *Nature Methods*. 2005;2(12):920.
39. Mantripragada VP, Jayasuriya AC. Bone regeneration using injectable BMP-7 loaded chitosan microparticles in rat femoral defect. *Materials Science & Engineering.C, Materials For Biological Applications*. 2016;63:596.

40. Li J, Xu Q, Teng B, Yu C, Li J, Song L, et al. Investigation of angiogenesis in bioactive 3-dimensional poly(d,l-lactide-co-glycolide)/nano-hydroxyapatite scaffolds by in vivo multiphoton microscopy in murine calvarial critical bone defect. *Acta Biomaterialia*. 2016;42:389.
41. Combs CA, Shroff H. Fluorescence Microscopy: A Concise Guide to Current Imaging Methods. *Current Protocols In Neuroscience*. 2017;79:2.1.25.
42. Yin L, Yang S, He M, Chang Y, Wang K, Zhu Y, et al. Physicochemical and biological characteristics of BMP-2/IGF-1-loaded three-dimensional coaxial electrospun fibrous membranes for bone defect repair. *J Mater Sci Mater Med*. 2017;28(6):1.
43. Falati S, Gross P, Merrill-Skoloff G, Furie BC, Furie B. Real-time in vivo imaging of platelets, tissue factor and fibrin during arterial thrombus formation in the mouse. *Nat Med*. 2002;8(10):1175.
44. Hillman EM. Optical brain imaging in vivo: techniques and applications from animal to man. *J Biomed Opt*. 2007;12(5):051402.
45. Juavinett AL, Nauhaus I, Garrett ME, Zhuang J, Callaway EM. Automated identification of mouse visual areas with intrinsic signal imaging. *Nature Protocols*. 2017;12(1):32.
46. Lu HD, Chen G, Cai J, Roe AW. Intrinsic signal optical imaging of visual brain activity: Tracking of fast cortical dynamics. *Neuroimage*. 2017;148:160.
47. Okada T, Takahashi S, Ishida A, Ishigame H. In vivo multiphoton imaging of immune cell dynamics. *Pflugers Archiv: European Journal Of Physiology*. 2016;468(11-12):1793.
48. Lefort C. A review of biomedical multiphoton microscopy and its laser sources. *Journal of Physics: D Applied Physics*. 2017;50(42):1.
49. Cromeey B, McDaniel A, Matsunaga T, Vagner J, Kieu KQ, Banerjee B. Pancreatic cancer cell detection by targeted lipid microbubbles and multiphoton imaging. *J Biomed Opt*. 2018;23(4):1.

50. Chu J, Shi P, Deng X, Jin Y, Liu H, Chen M, et al. Dynamic multiphoton imaging of acellular dermal matrix scaffolds seeded with mesenchymal stem cells in diabetic wound healing. *Journal Of Biophotonics*. 2018:e201700336.
51. Li J, Jahr H, Zheng W, Ren PG. Visualizing Angiogenesis by Multiphoton Microscopy In Vivo in Genetically Modified 3D-PLGA/nHAp Scaffold for Calvarial Critical Bone Defect Repair. *Journal Of Visualized Experiments: Jove*. 2017(127).
52. Fan Y, Xia Y, Zhang X, Sun Y, Tang J, Zhang L, et al. Optical coherence tomography for precision brain imaging, neurosurgical guidance and minimally invasive theranostics. *BioScience Trends*. 2018;12(1):12.
53. Fujimoto JG, Pitris C, Boppart SA, Brezinski ME. Optical coherence tomography: an emerging technology for biomedical imaging and optical biopsy. *Neoplasia*. 2000;2(1-2):9.
54. Atry F, Frye S, Richner TJ, Brodnick SK, Soehartono A, Williams J, et al. Monitoring Cerebral Hemodynamics Following Optogenetic Stimulation via Optical Coherence Tomography. *IEEE Transactions on Biomedical Engineering*. 2015;62(2):766.
55. Pan Y, You J, Volkow ND, Park K, Du C. Ultrasensitive detection of 3D cerebral microvascular network dynamics in vivo. *Neuroimage*. 2014;103:492.
56. Yue S, Lee PD, Poologasundarampillai G. Synchrotron X-ray microtomography for assessment of bone tissue scaffolds. *J Mater Sci Mater Med*. 2010;21(3):847.
57. Uhrig BA, Boerckel JD, Willett NJ, Li MT, Huebsch N, Guldberg RE. Recovery from hind limb ischemia enhances rhBMP-2-mediated segmental bone defect repair in a rat composite injury model. *Bone*. 2013;55(2):410.
58. Udagawa A, Sato S, Hasuike A, Kishida M, Arai Y, Ito K. Micro- CT observation of angiogenesis in bone regeneration. *Clin Oral Implants Res*. 2013;24(7):787.
59. Zou D, Zhang Z, He J, Zhang K, Ye D, Han W, et al. Blood vessel formation in the tissue-engineered bone with the constitutively active form of HIF-1a mediated BMSCs. *Biomaterials*. 2012;33(7):2097.

60. Rege A, Thakor NV, Rhie K, Pathak AP. In vivo laser speckle imaging reveals microvascular remodeling and hemodynamic changes during wound healing angiogenesis. *Angiogenesis*. 2012;15(1):87.
61. Meisner JK, Sumer S, Murrell KP, Higgins TJ, Price RJ. Laser speckle flowmetry method for measuring spatial and temporal hemodynamic alterations throughout large microvascular networks. *Microcirculation (New York, N.Y.: 1994)*. 2012;19(7):619.
62. Senarathna J, Rege A, Li N, Thakor NV. Laser Speckle Contrast Imaging: theory, instrumentation and applications. *IEEE Reviews In Biomedical Engineering*. 2013;6:99.
63. Dragojevic T, Bronzi D, Varma HM, Valdes CP, Castellvi C, Villa F, et al. High-speed multi-exposure laser speckle contrast imaging with a single-photon counting camera. *Biomedical Optics Express*. 2015;6(8):2865.
64. Cheng H, Duong TQ. Simplified laser-speckle-imaging analysis method and its application to retinal blood flow imaging. *Opt Lett*. 2007;32(15):2188.
65. Mehndiratta A, MacIntosh BJ, Crane DE, Payne SJ, Chappell MA. A control point interpolation method for the non-parametric quantification of cerebral haemodynamics from dynamic susceptibility contrast MRI. *Neuroimage*. 2013;64:560.
66. Shin KE, Ahn KJ, Choi HS, Jung SL, Kim BS, Jeon SS, et al. DCE and DSC MR perfusion imaging in the differentiation of recurrent tumour from treatment-related changes in patients with glioma. *Clin Radiol*. 2014;69(6):e264.
67. Boxerman JL, Ellingson BM, Jeyapalan S, Elinzano H, Harris RJ, Rogg JM, et al. Longitudinal DSC-MRI for Distinguishing Tumor Recurrence From Pseudoprogression in Patients With a High-grade Glioma. *American Journal Of Clinical Oncology*. 2017;40(3):228.
68. Livne M, Madai VI, Brunecker P, Zaro-Weber O, Moeller-Hartmann W, Heiss WD, et al. A PET-Guided Framework Supports a Multiple Arterial Input Functions Approach in DSC-MRI in Acute Stroke. *Journal Of Neuroimaging: Official Journal Of The American Society Of Neuroimaging*. 2017;27(5):486.

69. Beaumont M, DuVal MG, Loai Y, Farhat WA, Sandor GK, Cheng HL. Monitoring angiogenesis in soft-tissue engineered constructs for calvarium bone regeneration: an in vivo longitudinal DCE-MRI study. *NMR Biomed.* 2010;23(1):48.
70. Hudlicka O. Is physiological angiogenesis in skeletal muscle regulated by changes in microcirculation? *Microcirculation* (New York, N.Y.: 1994). 1998;5(1):7.
71. Ashkanian M, Gjedde A, Mouridsen K, Vafae M, Hansen KV, Østergaard L, et al. Carbogen inhalation increases oxygen transport to hypoperfused brain tissue in patients with occlusive carotid artery disease: Increased oxygen transport to hypoperfused brain. *Brain Res.* 2009;1304:90.
72. Egginton S, Hussain A, Hall-Jones J, Chaudhry B, Syeda F, Glen KE. Shear stress-induced angiogenesis in mouse muscle is independent of the vasodilator mechanism and quickly reversible. *Acta Physiologica.* 2016;218(3):153.
73. Macey PM, Woo MA, Harper RM. Hyperoxic brain effects are normalized by addition of CO<sub>2</sub>. *Plos Medicine.* 2007;4(5):e173.
74. Kalchenko V, Israeli D, Kuznetsov Y, Harmelin A. Transcranial optical vascular imaging (TOVI) of cortical hemodynamics in mouse brain. *Scientific Reports.* 2014;4:5839.
75. Derlin T, Granwald V, Steinbach J, Wester H, Ross TL. Molecular Imaging in Oncology Using Positron Emission Tomography. *Deutsches Aerzteblatt International.* 2018;115(11):175.
76. Sapoznik E, Niu G, Zhou Y, Murphy SV, Soker S. Fluorescent Cell Imaging in Regenerative Medicine. *Biomedical Engineering And Computational Biology.* 2016;7:29.
77. Samuel R, Daheron L, Liao S, Vardam T, Kamoun WS, Batista A, et al. Generation of functionally competent and durable engineered blood vessels from human induced pluripotent stem cells. *Proc Natl Acad Sci U S A.* 2013;110(31):12774.
78. Chi C, Du Y, Ye J, Kou D, Qiu J, Wang J, et al. Intraoperative imaging-guided cancer surgery: from current fluorescence molecular imaging methods to future multi-modality imaging technology. *Theranostics.* 2014;4(11):1072.

79. Sheyn D, Cohn Yakubovich D, Kallai I, Su S, Da X, Pelled G, et al. PTH promotes allograft integration in a calvarial bone defect. *Molecular Pharmaceutics*. 2013;10(12):4462.
80. Kirsch M, Wannez S, Thibaut A, Laureys S, Brichant JF, Bonhomme V. Positron Emission Tomography: Basic Principles, New Applications, and Studies Under Anesthesia. *Int Anesthesiol Clin*. 2016;54(1):109.
81. Petri M, Namazian A, Wilke F, Ettinger M, Stabig T, Brand S, et al. Repair of segmental long-bone defects by stem cell concentrate augmented scaffolds: a clinical and positron emission tomography--computed tomography analysis. *Int Orthop*. 2013;37(11):2231.
82. Haralampieva D, Betzel T, Dinulovic I, Salemi S, Stoelting M, Kramer SD, et al. Noninvasive PET Imaging and Tracking of Engineered Human Muscle Precursor Cells for Skeletal Muscle Tissue Engineering. *Journal Of Nuclear Medicine: Official Publication, Society Of Nuclear Medicine*. 2016;57(9):1467.
83. Kemerink M, Dierichs TJ, Dierichs J, Huynen H, Wildberger JE, van Engelshoven JM, et al. The application of x-rays in radiology: from difficult and dangerous to simple and safe. *Am J Roentgenol*. 2012;198(4):754.
84. van Lenthe GH, Hagenmuller H, Bohner M, Hollister SJ, Meinel L, Muller R. Nondestructive micro-computed tomography for biological imaging and quantification of scaffold-bone interaction in vivo. *Biomaterials*. 2007;28(15):2479.
85. Kim SH, Suh HS, Cho MH, Lee SY, Kim TS. Finite element simulation of ultrasound propagation in bone for quantitative ultrasound toward the diagnosis of osteoporosis. *Conference Proceedings: Annual International Conference Of The IEEE Engineering In Medicine And Biology Society. IEEE Engineering In Medicine And Biology Society. Annual Conference*. 2009;2009:436.
86. Ventura M, Boerman OC, de Korte C, Rijpkema M, Heerschap A, Oosterwijk E, et al. Preclinical imaging in bone tissue engineering. *Tissue Engineering. Part B, Reviews*. 2014;20(6):578

88. Briers JD, Fercher AF. Retinal blood-flow visualization by means of laser speckle photography. *Invest Ophthalmol Vis Sci.* 1982;22(2):255.
89. Gal TJ. Nunn's Applied Respiratory Physiology. 5th ed. *Anesthesia & Analgesia.* 2000 Apr;90(4):1009.
90. Yoon S, Zuccarello M, Rapoport RM. pCO<sub>2</sub> and pH regulation of cerebral blood flow. *Frontiers In Physiology.* 2012;3:365.
91. Schneider CA, Rasband WS, Eliceiri KW. NIH Image to ImageJ: 25 years of image analysis. *Nature Methods.* 2012;9(7):671.
92. Thavenaz P, Ruttimann UE, Unser M. A pyramid approach to subpixel registration based on intensity. *IEEE Transactions On Image Processing: A Publication Of The IEEE Signal Processing Society.* 1998;7(1):27.
93. Sato Y, Nakajima S, Shiraga N, Atsumi H, Yoshida S, Koller T, et al. Three-dimensional multi-scale line filter for segmentation and visualization of curvilinear structures in medical images. *Med Image Anal.* 1998;2(2):143.
94. Arganda-Carreras I, Fernandez-Gonzalez R, Munoz-Barrutia A, Ortiz-De-Solorzano C. 3D reconstruction of histological sections: Application to mammary gland tissue. *Microsc Res Tech.* 2010;73(11):1019.
95. Leymarie F, Levine MD. Fast raster scan distance propagation on the discrete rectangular lattice. *CVGIP: Image Understanding.* 1992;55:84.
96. Kusumbe AP, Ramasamy SK, Starsichova A, Adams RH. Sample preparation for high-resolution 3D confocal imaging of mouse skeletal tissue. *Nature Protocols.* 2015;10(12):1904-14.
97. Wang Y, Wan C, Deng L, Liu X, Cao X, Gilbert SR, et al. The hypoxia-inducible factor alpha pathway couples angiogenesis to osteogenesis during skeletal development. *J Clin Invest.* 2007;117(6):1616-26.

98. Ramasamy SK, Kusumbe AP, Schiller M, Zeuschner D, Bixel MG, Milia C, et al. Blood flow controls bone vascular function and osteogenesis. *Nature Communications*. 2016;7:13601.

99. Sun J, Jiao K, Niu L, Jiao Y, Song Q, Shen L, et al. Intrafibrillar silicified collagen scaffold modulates monocyte to promote cell homing, angiogenesis and bone regeneration. *Biomaterials*. 2017;113:203-16.



## **CURRICULUM VITAE**

Adam Luis Mendez was born in Austin, Texas on November 24, 1995. He attended Johns Hopkins University from August 2014 until May 2017 to complete his Bachelor's in Science in Chemical and Biomolecular Engineering. He then remained at Hopkins an additional year to complete his Masters in Science in Chemical and Biomolecular Engineering. His research has focused on cancer cell lines, tissue engineering, and functional imaging.